Decohesion Kinetics of PEDOT:PSS Conducting Polymer Films

*Stephanie R. Dupont, Fernando Novoa, Eszter Voroshazi, and Reinhold H. Dauskardt**

The highly conductive polymer PEDOT:PSS is a widely used hole transport layer and transparent electrode in organic electronic devices. To date, the mechanical and fracture properties of this conductive polymer layer are not well understood. Notably, the decohesion rate of the PEDOT:PSS layer and its sensitivity to moist environments has not been reported, which is central in determining the lifetimes of organic electronic devices. Here, it is demonstrated that the decohesion rate is highly sensitive to the ambient moisture content, temperature, and mechanical stress. The kinetic mechanisms are elucidated using atomistic bond rupture models and the decohesion process is shown to be facilitated by a chemical reaction between water molecules from the environment and strained hydrogen bonds. Hydrogen bonds are the predominant bonding mechanism between individual PEDOT:PSS grains within the layer and cause a significant loss in cohesion when they are broken. Understanding the decohesion kinetics and mechanisms in these films is essential for the mechanical integrity of devices containing PEDOT:PSS layers and yields general guidelines for the design of more reliable organic electronic devices.

1. Introduction

Conductive polymers have enabled the development of many flexible electronic devices, including organic light emitting diodes (OLEDs), organic photovoltaics (OPVs) and organic thin film transistors (OTFTs).[1–3] The compatibility of poly(3,4-ethylenedioxythiophene) poly(styrene-sulfonate) (PEDOT:PSS) with a variety of printing techniques, along with its high visible light transmission and high conductivity, has made it the most commonly used hole transport or electrode layer in these devices. However, polymers are often more mechanically fragile than their metal counterparts, and devices containing these materials have a high tendency for mechanical failure associated with adhesive and cohesive debonding of the polymer layer. The critical adhesion or cohesion debond energy, G_c (J m^{-2}), can be quantified in terms of the macroscopic work of fracture per unit area to separate two layers or break a layer.[4] G_c values of polymer layers and interfaces are generally reported in adhesion and cohesion studies of polymer solar cells,[5–9] but they do not provide information regarding the time-dependent sensitivity of these parameters to the environment or the debonding kinetics.

No understanding currently exists for the decohesion kinetics of conjugated polymers and more specifically PEDOT:PSS, particularly when exposed to moist environments. Time-dependent decohesion processes typically involve the interaction of strained atomic bonds at the debond tip and a chemical species in the environment.[4,10–14] However, it is important to note that not all polymers are susceptible to moisture assisted decohesion, and this is the first report which studies this process in PEDOT:PSS. Decohesion may be driven by the residual stresses, thermomechanical cycling and mechanical or vibrational loading. Moisture may be present in the materials, in operating environments or accumulated during processing steps which involve exposure to aqueous environments. Decohesion kinetics can be studied by measuring the decohesion rate, da/dt, in terms of the applied driving force, G, using a thin-film decohesion technique. The debond growth rate curves typically result in a sigmoidal shape where changes in slope indicate a change in the rate limiting step for debond advancement.[12,14,15] Different regions have been identified and well documented.[10,16,17]

Here, we explore the decohesion kinetics in the PEDOT:PSS layer under systematically varied environmental conditions with changing relative humidity and temperature. PEDOT:PSS was integrated as the hole transport layer in an inverted OPV, but the results and degradation mechanisms are independent of the device structure and should be valid for any device containing PEDOT:PSS layers. First, we show the existence of time-dependent debonding in the PEDOT:PSS layer at stresses well below those required for critical failure. We demonstrate how the decohesion rate is significantly influenced by moisture content and temperature along with mechanical loads. Then, we elaborate on degradation mechanisms leading to the moisture-assisted decohesion, which involves the interaction of water molecules from the environment with strained hydrogen bonds in the PEDOT:PSS layer at the debond tip (**Figure 1**). Finally, we use atomistic kinetic models to further elucidate the moisture-assisted

S. R. Dupont, F. Novoa, Prof. R. H. Dauskardt
Department of Materials Science and Engineering
Stanford University
Stanford, CA 94305-2205, USA
E-mail: dauskardt@stanford.edu
Dr. E. Voroshazi
IMEC vzw, Kapeldreef 75, 3000, Leuven, Belgium

DOI: 10.1002/adfm.201302174

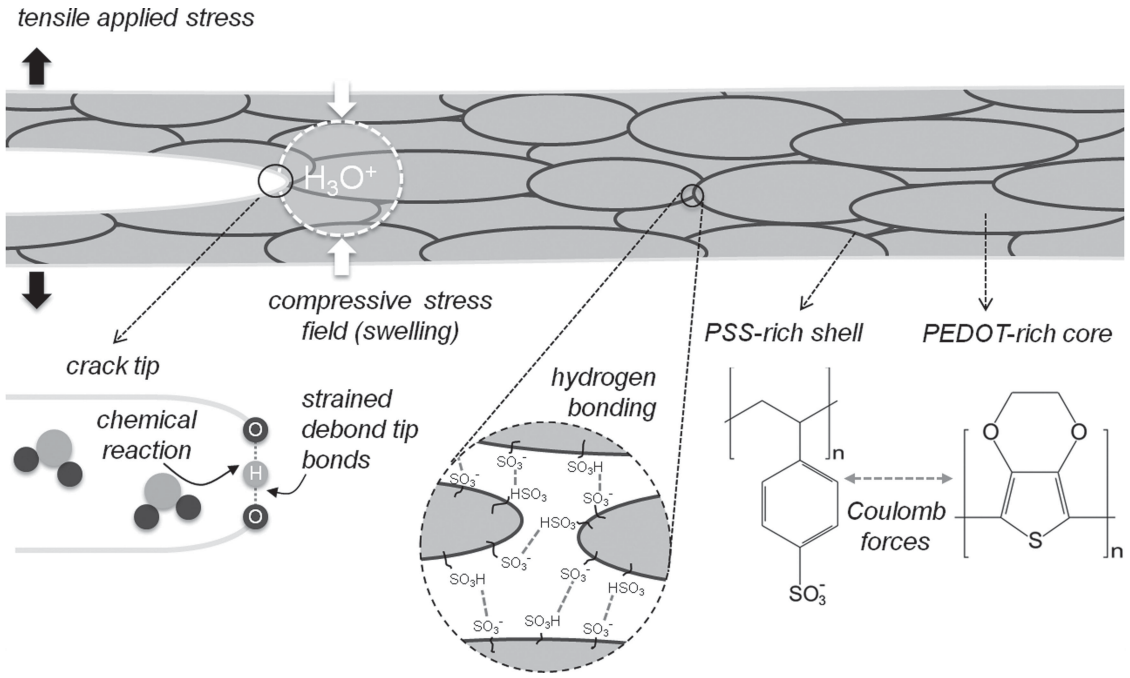

Figure 1. Illustration of the PEDOT:PSS layer. A thin-film of PEDOT:PSS consist of grains with a PEDOT-rich core and PSS-rich shell held together by Coulomb forces. The individual grains are held together by hydrogen bonds. The figure also shows the decohesion mechanism enabled by a stress-dependent chemical reaction between the water molecules and strained hydrogen bonds at the debond tip and the development of a compressive stress field due to the absorption of water.

decohesion mechanisms. Understanding the decohesion kinetics and the degradation mechanisms provides valuable insights regarding the mechanical integrity and stability of devices containing PEDOT:PSS layers.

2. Results and Discussion

2.1. Decohesion rate

The decohesion rates, da/dt, in the PEDOT:PSS layer were measured as a function of the applied debond driving force, G, using a thin-film delamination technique. The decohesion rate curves from tests performed over a wide range of moisture contents and a fixed temperature of 22 °C are shown in **Figure 2**. Prior to testing, an adhesive pre-crack was induced at the P3HT:PCBM/PEDOT:PSS interface. The very steep debond growth rate curve, measured in a dry or 5% relative humidity (R.H.) environment, corresponds to some degree of adhesive debond growth at the interface of the poly sx(3-hexyl) thiophene: [6,6]-phenyl-C_{61}-butyric acid methyl ester (P3HT:PCBM) and PEDOT:PSS. The measured G values were found to be close to the critical adhesion energy of this interface, which will be discussed in greater detail below. In a moist environment (40, 60, and 80% R.H.), debond growth rate curves over a wide range of G values were obtained. The synergistic

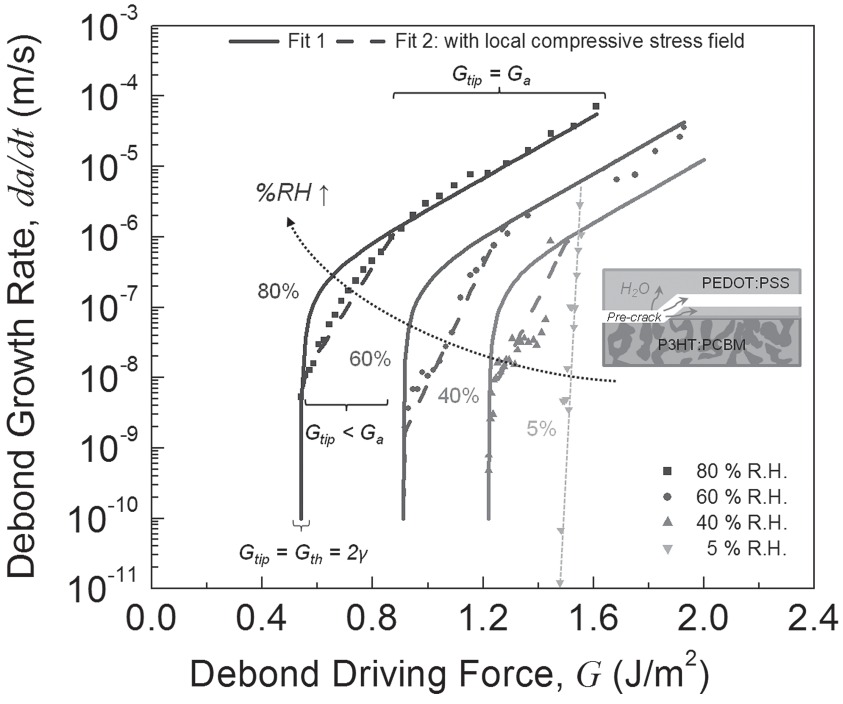

Figure 2. Debond growth rate curves. The decohesion rate, da/dt (m s^{-1}), as a function of debond driving force, G (J m^{-2}) at a constant temperature of 22 °C and varying moisture content. The straight lines (Fit 1) represent fits to the data using atomic reaction rate kinetics, given by Equation 4. The dashed lines (Fit 2) accommodate for the compressive stress field that reduces the effective driving force at the debond tip G_{tip} induced by water uptake.

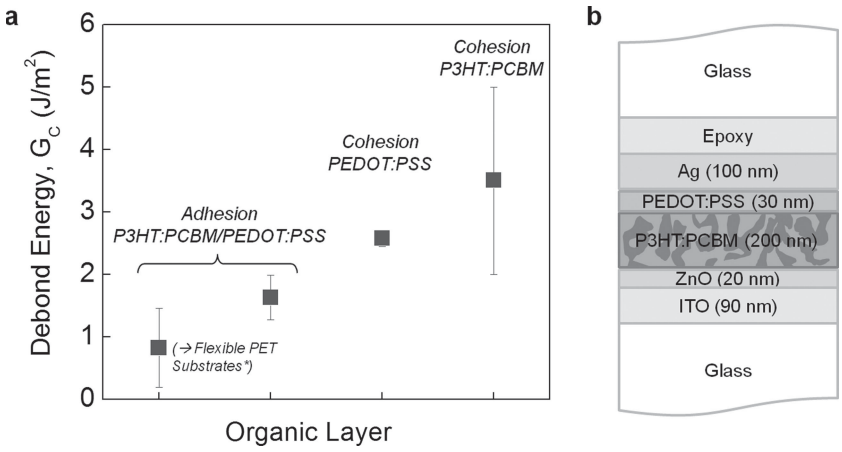

Figure 3. Debond energy of organic electronic materials and interfaces. a) The adhesion and cohesion energy values, G_c (J m^{-2}), of different organic layers present in an inverted polymer solar cell. These adhesion values correspond to solar cell samples made on flexible PET substrates, while all the others are made on square glass substrates. b) The structure of the DCB specimen, build from a typical inverted polymer solar cell.

effect of applied mechanical loads and moisture caused debond deflection and propagation in the 30 nm PEDOT:PSS layer, which we refer to as moisture-assisted decohesion. Up to several millimeters of cohesive failure in the PEDOT:PSS layer was observed for debonding in a 40, 60, and 80% R.H. environment. More details on the characterization and localization of the debond path are discussed below.

Figure 2 depicts the significant effect of moisture content on the position of the decohesion rate curves. Increasing humidity shifted the entire curves to lower G values, indicating accelerated moisture-assisted decohesion in increased moisture content environments. The lowest driving energy measured for debond extension at 22 °C was 0.54 J m^{-2}. To compare these driving force values to the critical adhesion and cohesion energy values, we measured the G_c values of relevant organic layers in an OPV device, shown in **Figure 3**a. The adhesion energy of the interface between the PEDOT:PSS and P3HT:PCBM was found to be the lowest with values ranging from 0 to 2 J m^{-2}, depending on the P3HT:PCBM composition ratio, annealing conditions and other processing parameters.[5,6,8] The cohesion energy of the PEDOT:PSS layer was measured to be about 2.5 J m^{-2}. The cohesion energy of P3HT:PCBM in conventional polymer solar cells was reported in the range of 2 to 5 J m^{-2} and included here for comparison. Further details are reported elsewhere.[7]

To precisely locate the debond path in the three aforementioned scenarios (cohesive in the PEDOT:PSS layer, cohesive in the P3HT:PCBM layer or adhesive at the P3HT:PCBM/PEDOT:PSS interface) and distinguish PEDOT:PSS from P3HT:PCBM, several surface analysis techniques were used. Contact angle (CA)'s on the debonded surfaces were measured and compared to the CA's of reference PEDOT:PSS and P3HT:PCBM layers. The CA's of P3HT:PCBM and PEDOT:PSS were measured in the range of 80–85° and 28–33°, respectively.

To further elucidate the debond path, detailed X-ray photoelectron spectroscopy (XPS) characterization was used. The XPS survey scans and high-resolution scans of adhesive failure between PEDOT:PSS and P3HT:PCBM are shown in **Figure 4**a–d. XPS revealed 85.7 at% carbon (C), 7.1 at% sulfur (S), 6.7 at% oxygen (O), and 0.5 at% silver (Ag) at the PEDOT:PSS interface and 92.8 at% carbon, 6.4 at% sulfur and 0.8 at% oxygen at the P3HT:PCBM interface. Both PEDOT:PSS (Figure 1) and P3HT:PCBM are composed exclusively of C, O and S atoms, and as observed in this example the only difference between the P3HT:PCBM and PEDOT:PSS is the slightly higher concentration of oxygen on the PEDOT:PSS surface. However, high-resolution XPS scans around the S_{2p} core level (155–175 eV) demonstrate a much clearer differentiation between P3HT:PCBM and PEDOT:PSS due to the difference in binding energy. All four organic materials (P3HT, PCBM, PEDOT, and PSS) contain single sulfur-oxygen and single sulfur-carbon bonds, which are represented by the double peak around 164 eV. PSS is the only one that has double sulfur oxygen bonds due to the presence of sulfonate groups (S=O), that result in a unique peak around 168 eV. Similarly, cohesive failure in the P3HT:PCBM and PEDOT:PSS layers was determined by CA measurements and XPS characterization.

The ratio of the areas under the 168 eV to 164 eV peaks can qualitatively be understood as the ratio of the PSS (168 eV) to the PEDOT (164 eV) content. Previously published results reported the existence of a PSS-rich layer at the air interface, or the interface with the Ag electrode.[18,19] In the present study, we were able to measure this ratio for the first time at the opposite interface. The area under the 164 eV peak was found to be much larger than the area under the 168 eV peak, revealing a PEDOT rich layer towards the bottom of the layer (Figure 4c). This confirms earlier findings on phase separation in spin-coated PEDOT:PSS with a PSS-rich layer towards the air interface and a PEDOT-rich layer near bottom.[19]

During moisture-assisted debonding, cohesive failure in the PEDOT:PSS layer was observed, as introduced above. XPS characterization on both of the moisture-assisted decohesion surfaces revealed 60–70 at% C, 5–7 at% S, 18–24 at% O and 1–5 at% Ag, shown in Figure 4e,f. The thickness of the remaining PEDOT:PSS layer on top of the P3HT:PCBM layer after debonding was measured to be between 15–25 nm by determining the step height between the pre-crack region and moisture-assisted region with atomic force microscopy (AFM). An example AFM image of an 18 nm PEDOT:PSS thick layer is given in **Figure 5**a. The PEDOT:PSS layer remaining on the opposite site of the crack was determined to be 5–15 nm thick by XPS depth profiling at an average sputter rate of 5 nm PEDOT:PSS/min (Figure 5b). The rate was calculated by recording the time to sputter through multiple 30 ± 5 nm thick PEDOT:PSS layers.

As mentioned earlier, the lowest driving energy for debond extension was measured as 0.54 J m^{-2}. This was a reduction of 70% from the critical interface adhesion of 1.8 J m^{-2} and even more significantly, an 80% reduction from the critical cohesion energy of the PEDOT:PSS of 2.5 J m^{-2}. The presence of debonding at applied driving energies significantly below G_c has important implications for the long-term reliability of

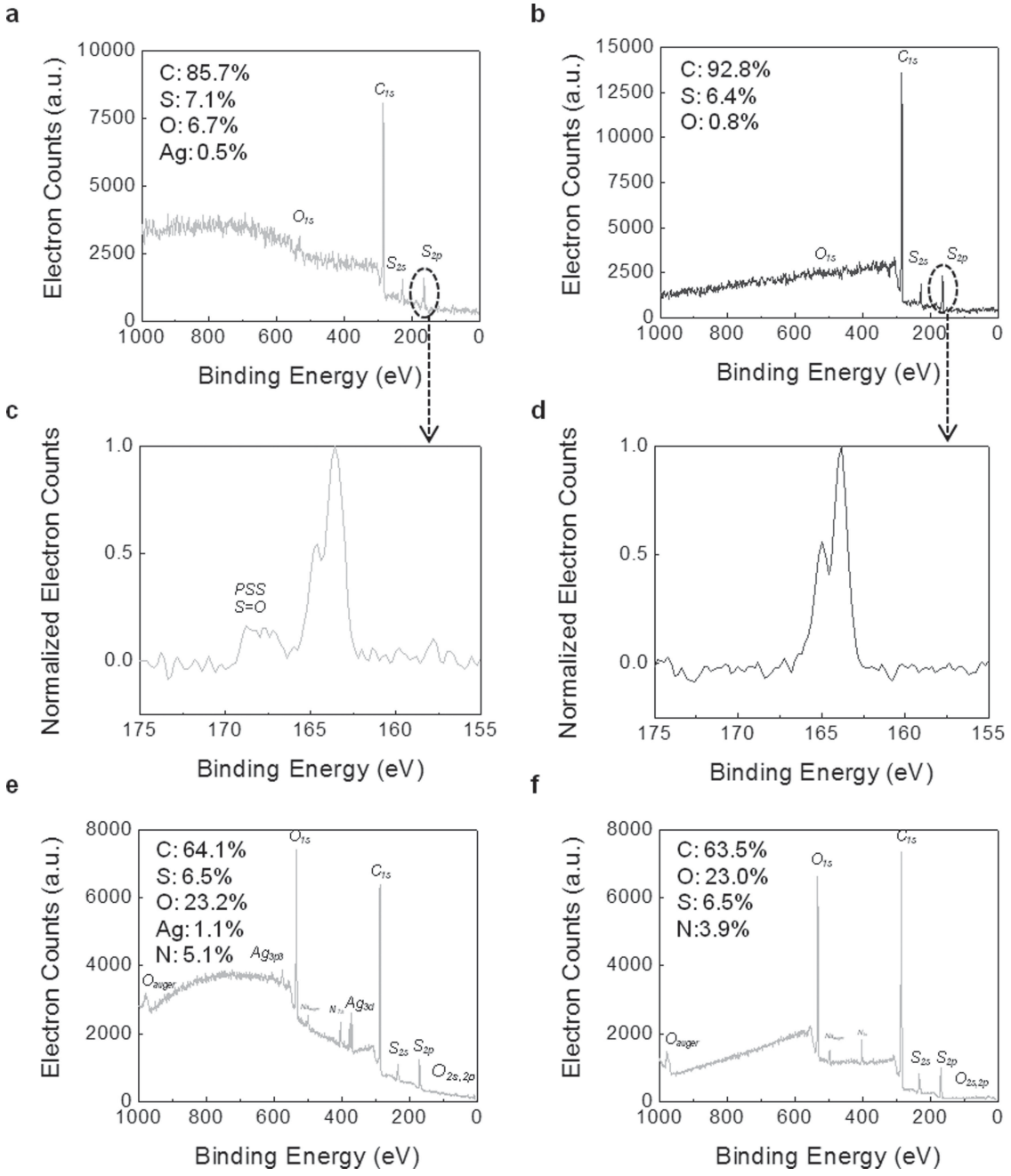

Figure 4. XPS spectra of the debonded surfaces. The XPS survey spectra of the adhesively debonded surfaces a) PEDOT:PSS and b) P3HT:PCBM, and e,f) the cohesively debonded PEDOT:PSS surfaces with a large oxygen concentration. High-resolution XPS scans around the S_{2p} core level on the c) PEDOT:PSS and d) P3HT:PCBM debond surfaces.

devices containing PEDOT:PSS layers prone to time dependent debonding. In order to increase the lifetime of these devices, it is important to understand the physical mechanism causing moisture-assisted decohesion.

2.2. Mechanisms

PEDOT:PSS is a water soluble polyelectrolyte complex with an excess of PSS and is held together by strong coulomb forces between the polyanion PSS and polycation PEDOT (Figure 1). A number of publications have described a grain-like morphology in solution and lentil-like morphology in a dry film, both with a PEDOT-rich core and PSS-rich shell.[20,21] The average diameter and thickness of the grains was reported in the range of 30–50 nm and 5–10 nm, respectively. The individual grains are primarily held together by hydrogen bonds formed between the sulfonate groups of PSS (Figure 1). At a fixed temperature and pressure, the hydrogen bond strength decreases as

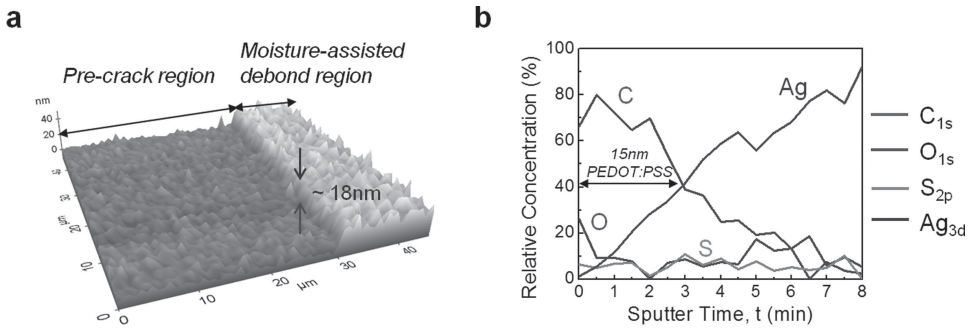

Figure 5. Cohesive failure path in the PEDOT:PSS layer. a) An AFM image of debonded surface illustrating the step height between the adhesive pre-crack region and the moisture-assisted decohesion region. b) XPS depth profile through the debonded surface measuring a 15 nm thick PEDOT:PSS layer on the Ag electrode.

the hydrogen bond length increases. During moisture-assisted decohesion, the bonds at the debond tip are strained, which weakens the hydrogen bond forces. The water molecules near the debond tip may react with these weakened hydrogen bonds through a chemical reaction.[22]

$$H_2O + PSS\,(HSO_3) \rightarrow H_3O^+ + PSS(SO_3)^- \quad (1)$$

This mechanism facilitates debond propagation through the PEDOT:PSS film in moist environments, enabled by the synergistic effect of mechanical loads and water molecules (Figure 1). The occurrence of the chemical reaction given in Equation 1 and thus the absorption of water during debond propagation was also observed by the increased oxygen concentration from 6–7 at% O on the PEDOT:PSS interfacial debond surface to 18–24 at% O on the moisture-assisted debonded surfaces (Figure 4). Since the decohesion mechanism is largely attributed to the hydrogen bonds that are predominant in bonding the individual PEDOT:PSS grains within the layer, we believe similar degradation mechanisms are expected to happen in many other polymer complexes held together by weak hydrogen bonds. Examples of such common conductive polymers are polypyrrole with polyimide, polyvinyl alcohol, and polyurethane blends and polyaniline-based blends.[23–25]

At each moisture content, a threshold G_{TH} was measured, denoted by the vertical region of the curves at low decohesion rates, which shifted to lower debond driving energies as the moisture content increased. Plotting the G_{TH} values versus the natural logarithm of the partial pressure of water vapor, yields a linear relationship (**Figure 6**a). This behavior is consistent with that expected for a stress-enabled chemical reaction occurring at the debond tip. For a simple bond-rupture reaction of the sort

$$nH_2O + B \rightarrow B^* \quad (2)$$

G_{TH} is given by the relevant chemical potential:[14,15]

$$\begin{aligned} G_{TH} &= 2\gamma = Nu_o = N\left[\mu_{B^*} - \mu_B - n\mu_{H_2O}\right] \\ &= N\left[\alpha(T) - nRT\ln P_{H_2O}\right] \end{aligned} \quad (3)$$

where the reaction order n indicates the number of water molecules, B represents an unbroken bond and B^* represents a

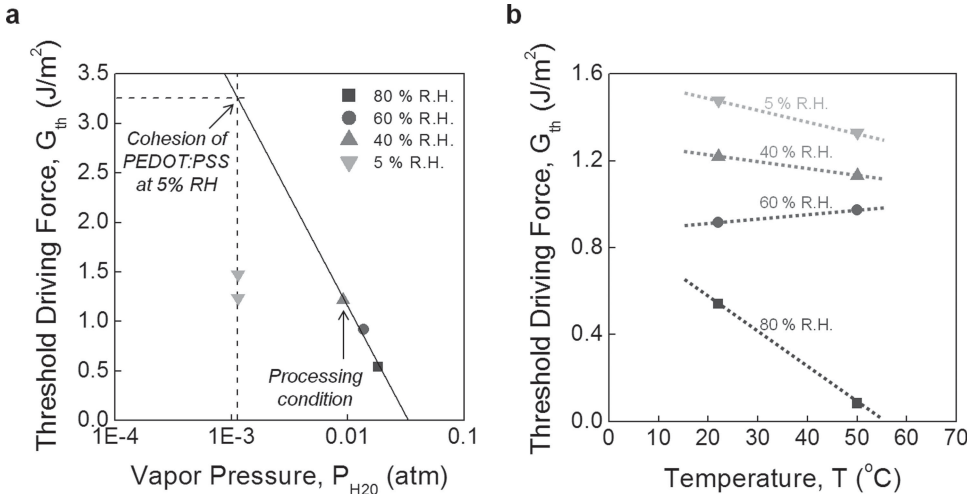

Figure 6. Threshold driving force. The threshold driving force, G_{TH} (J m^{-2}), for varying moisture content as a function of the a) water vapor pressure, P_{H2O} (atm) and b) temperature, T (°C).

broken bond, N is the number of bonds per unit area, T is the absolute temperature, and P_{H2O} is the partial pressure of water vapor. Equation 3 indicates that the position of the threshold driving force of a stress-enabled chemical reaction in Equation 2 will shift with the logarithm of the partial pressure of water vapor.

The value of G_{TH} measured at 5% R.H. did not follow this logarithmic behavior, because it is associated with adhesive and not cohesive failure. By extrapolating the logarithmic trend in Figure 6b, the G_c of the PEDOT:PSS layer in a 5% R.H. environment is expected to be at least 3.25 J m^{-2}. This is larger than the measured G_c for cohesive failure in the PEDOT:PSS layer, prepared and measured at 40% R.H. (Figure 3b), due to PEDOT:PSS cohesion loss in increased moisture content environments.[26]

2.3. Modeling Decohesion Kinetics

According to atomic reaction rate kinetics, the decohesion growth rate, controlled by bond rupture and healing effects, can be given by[14,15]

$$da/dt = v_o \sinh\left[\frac{G_{tip} - 2\gamma}{\eta}\right] \quad (4)$$

where the v_o and η are macroscopic debond growth parameters related to the local atomic and chemical environment, G_{tip} is the applied driving force at the debond tip, and 2γ is the intrinsic resistance to bond rupture for the given material in the reactive environment, also known as the threshold driving force, G_{TH}. The atomic reaction rate model in Equation 4 has been successfully used to fit the reaction-controlled region data for tests conducted on a wide range of bulk glasses, other brittle inorganic materials and polymer/metal interfaces.[11,13,15,27,28] In this study, we fitted Equation 4 to the data, using G_{TH} values given in Figure 6, shown in Figure 2 as Fit 1, and found values for the macroscopic debond growth parameters $v_o \approx 4.6 \times 10^{-7}$ m/s and $\eta \simeq 0.195\,\mathrm{J/m^2}$. The energy required to create a single broken bond is given by[15]

$$u_o = \frac{4\gamma k T}{\eta} \quad (5)$$

We calculated u_o; 0.32 eV, 0.24 eV, and 0.14 eV, in 40% R.H., 60% R.H., and 80% R.H. environments, respectively and concluded that the strength of an individual hydrogen bond decreased with increasing moisture content, due to increased hydrogen bond length. These values are comparable to the activation energy needed to break hydrogen bonds, which range between 0.1 eV and 0.4 eV.[29] Fit 1 represents the overall moisture-assisted decohesion behavior well, but overestimates the decohesion rate in the intermediate growth rate regime from 10^{-6} to 10^{-8} m s^{-1}. The deceleration in decohesion rate can be explained by generation of an additional compressive stress field near the debond tip.

In a moist environment, the hygroscopic PEDOT:PSS layer takes up water from its surroundings. The PEDOT:PSS grains swell, but are spatially confined, leading to a local compressive stress field near the debond tip (Figure 1). The change in film stresses alters the mechanical driving force at the debond tip, G_{tip}, which can be quantified using models to account for the effects of a region of material surrounding a debond that undergoes a dilatational strain.[30–34] G_{tip} can be expressed in terms of the stress intensity factor, K_{tip}, and the Young's modulus of the film, E_f, $by\, G_{tip} = K_{tip}^2/E_f$ *and* $K_{tip} = K_a - \Delta K$, where K_a is the applied stress intensity factor and ΔK is the change in the debond tip stress intensity factor due to the compressive zone

$$\Delta K = \frac{A\varepsilon_T E_f \sqrt{w}}{1 - \nu_f} \quad (6)$$

The constant A is related to the shape of the frontal zone, E_f is the Young's modulus of the PEDOT:PSS film, ν_f is the Poisson's ratio of the PEDOT:PSS film, ε_T is the stress-free transformation strain that would result if the film were not attached to the substrate, and w is height of the compressive zone.

The mechanical driving force near the debond tip, G_{tip}, in the intermediate growth rate regime is thus smaller than the applied driving force, G_a used in Fit 1, due to the formation of a compressive strain zone surrounding the debond tip. We have accordingly adapted Fit 1 with the effective G_{tip} values in the intermediate growth rate regime shown as Fit 2 (dashed lines) in Figure 2. For the scope of this work we have used $A = 0.37$[30], $\nu_f = 0.34$, and $E_f = 1.9$ *GPa*[26]. The height, *w*, was approximated by the diffusion depth of a one dimensional diffusion process with a constant concentration of water molecules at the edge, and was calculated proportional to the square root of time with a maximum value of half the layer thickness, 15 nm. We found values for the strain transformation, ε_T ; 6.0% for 80% R.H., 3.5% for 60% R.H., and 1.7% for 40% R.H. These ε_T are exactly 1.8 to 1.9 times larger than the out of plane strain measured in free standing PEDOT:PSS films.[35]

Note that the diffusion rate of the water molecules into the films was sufficiently slow that the effect of swelling was only important at intermediate decohesion rates (10^{-6}–10^{-8} m s^{-1}), where the water molecules had the time to diffuse into the PEDOT:PSS layer on both sides of the debond. At high decohesion rates, the effect of swelling was absent because the water molecules did not have enough time to diffuse into the PEDOT:PSS layer.

2.4. Effect of Temperature

Organic electronic devices, and especially photovoltaic modules, operate at elevated temperatures; therefore, we focus here on the effect of temperature on the decohesion rate. Nominal operating solar cell temperatures on the order of 40–50 °C are reported.[36] We measured decohesion rates at 50 °C over a wide range of moisture contents from 5 to 80% R.H., similarly to debonding at 22 °C. Again, increasing humidity shifted the entire decohesion rate curve to lower G values. The measured G_{TH} values at 22 °C and 50 °C are compared in Figure 6b. An overall shift to lower values at 50 °C is observed, which is attributed to the accelerated decohesion kinetics with increased temperature. At high temperature and high humidity, G_{TH} was found to be extremely low, which has a significant effect on the lifetime of devices operated in these conditions. Based on this plot, we concluded that moisture has a higher effect on reducing the G_{TH} rather than temperature. Small changes in moisture content may dramatically affect the cohesion of PEDOT:PSS which will have deleterious effects on the device reliability.

3. Conclusion

We demonstrated that PEDOT:PSS is susceptible to moisture-assisted decohesion. This time-dependent decohesion process occurred at mechanical stresses lower than those needed to fracture a layer, and therefore has implications on the long term stability of organic electronic devices containing these polymer layers. The moisture content in the environment and not the temperature was found to be the most important factor reducing the G_{TH} values and accelerating decohesion rate. Moisture-assisted decohesion was facilitated by a reaction between water molecules from the environment and strained hydrogen bonds at the debond tip in the PEDOT:PSS layer. Using atomistic kinetic models. we were further able to distinguish a deceleration in debond propagation at intermediate decohesion rates. The latter is attributed to water uptake creating a local compressive layer and therefore decreasing the effective driving force for decohesion. Since the decohesion mechanism is largely attributed to the hydrogen bonds that form the basis of the PEDOT:PSS film structure, we believe similar degradation mechanisms are expected to happen in any other polymer complex held together by weak hydrogen bonds. The findings on the decohesion rate and mechanism revealed in this paper are essential for the design of more reliable organic electronic devices.

4. Experimental Section

Inverted OPVs with ITO/ZnO/P3HT:PCBM/PEDOT:PSS/Ag structure were made on square glass substrates (Figure 3b). The details of the OPV sample preparation have been reported previously.[8,37] An identical glass substrate was bonded on top of the silver electrode using a brittle epoxy resulting in a square glass sandwich. Double cantilever beam (DCB) fracture specimens of 5 mm wide, 30 mm long, and 1.5 mm thick were machined using a high speed wafer saw with a resin blade. To prevent water coolant diffusing into the OPV structure during dicing and damaging the solar cell materials, trenches were cut on each side of square sandwich. Perfectly aligned trenches on the top and bottom glass substrates of the sandwiched structure made it easy to cleave individual DCB specimens prior to testing.

An initial crack or pre-crack of 10 mm long was introduced in the DCB specimen, by loading the sample under tensile in a thin-film cohesion testing system (Delaminator DTS, Menlo Park, CA) until an initial crack was naturally created. The sample was then loaded and unloaded to generate a pre-crack of desired length. Subsequently, the DCB specimens were loaded to a predetermined load under displacement control from which a load, P, versus displacement, Δ, curve was recorded. The fracture energy, G_c (J m^{-2}), was measured in terms of the critical value of the applied strain energy release rate, G. G_c can be expressed in terms of the critical load, P_c, at which debond growth occurs, the debond length a, the plain strain elastic modulus, E', of the substrates and the specimen dimensions; width, b and half-thickness, h. The fracture energy was calculated from[38]

$$G_c = \frac{12 P_c^2 a^2}{B^2 E' h^3}\left(1 + 0.64\frac{h}{a}\right)^2 \quad (7)$$

The debond length was measured directly under an optical microscope and also inferred from measurement of the elastic compliance, $d\Delta/dP$, using the compliance relationship:

$$a = \left(\frac{d\Delta}{dP} \times \frac{B E' h^3}{8}\right)^{1/3} - 0.64 \times h \quad (8)$$

All G_c testing was carried out in laboratory air environment at ≈25 °C and ≈40% R.H.

To study the decohesion kinetics under varying environmental conditions, the entire system was placed in a controlled environment at constant temperature (±1 °C) and relative humidity (±2% R.H.) after a 12 h equilibration period. The general method to measure the debond growth rates, da/dt, as a function of applied debond driving force, G, involves load relaxation techniques and compliance methods and has been described elsewhere.[4,38] Shortly, the fracture specimens were loaded to a predetermined load at which the displacement was fixed. Then, the naturally decreasing loads that resulted from debond extension were recorded. The later was calculated using specimen compliance

$$\frac{da}{dt} = \frac{-a_i \times P_i^{1/3}}{P^{4/3}}\frac{dP}{dt} \quad (9)$$

where a_i and p_i are the initial debond length and load, respectively. In this study, da/dt was measured at a temperature of 22 °C and 50 °C and moisture content ranging from 5% R.H. to 80% R.H. Time-dependent debonding was measured over several orders of magnitude from 10^{-4} m s^{-1} to 10^{-11} m s^{-1}, during which several millimeters of debond extension were observed.

Following mechanical testing, a survey X-ray photo spectroscopy (XPS, PHI 5000 Versaprobe) scan (0–1000 eV), taken at a 45° incident angle, was made of each of the fractured specimens using monochromatic Al Kα X-ray radiation at 1487 eV in order to characterize the surface chemistry and to help precisely locate the debond path. To minimize contamination, the samples were stored in a nitrogen (99%+) chamber and only exposed to ambient air (maximum 20 min) when transferred to the XPS vacuum chamber. Detailed high-resolution XPS scans around the S_{2p} core level (155–175 eV) were made for compositional analysis and further identification of the debond path. Contact angles (CA) (190, rame-hart) were measured with ethylene glycerol (ACROS Organics, 99%+) to further quantify the debond surface chemistry. XPS depth profiling, using Argon sputtering at 1 kV, 0.5 μA and a spot size of 2 mm × 2 mm, was used to quantify the thickness of the PEDOT:PSS layer. Atomic force microscopy (AFM) (XE-70, Park Systems) was used in a non-contact mode to measure the step height between the pre-debond and the moisture-assisted debond region to locate the debond path.

Acknowledgments

This research was supported by the Center for Advanced Molecular Photovoltaics (CAMP) supported by King Abdullah University of Science and Technology (KAUST) under award no. KUS-C1-015-21.

Received: June 27, 2013
Revised: August 23, 2013
Published online: October 17, 2013

[1] G. Li, V. Shrotriya, J. S. Huang, Y. Yao, T. Moriarty, K. Emery, Y. Yang, *Nat. Mater.* **2005**, *4*, 864–868.
[2] H. Sirringhaus, T. Kawase, R. H. Friend, T. Shimoda, M. Inbasekaran, W. Wu, E. P. Woo, *Science* **2000**, *290*, 2123–2126.
[3] B. W. D'Andrade, S. R. Forrest, *Adv. Mater.* **2004**, *16*, 1585–1595.
[4] R. Dauskardt, M. Lane, Q. Ma, N. Krishna, *Eng. Fract. Mech.* **1998**, *61*, 141–162.
[5] S. R. Dupont, E. Voroshazi, P. Heremans, R. H. Dauskardt , *Photovoltaic Specialists Conference (PVSC) 2012 38th IEEE* **2012**, 003259–003262.
[6] S. R. Dupont, M. Oliver, F. C. Krebs, R. H. Dauskardt, *Sol. Energ. Mat. Sol. C.* **2012**, *97*, 171–175.

[7] V. Brand, C. Bruner, R. H. Dauskardt, *Sol. Energ. Mat. Sol. C.* **2012**, *99*, 182–189.
[8] S. R. Dupont, E. Voroshazi, P. Heremans, R. H. Dauskardt, *Org. Electron.* **2013**, *14*, 1262–1270.
[9] M. Jorgensen, K. Norrman, S. A. Gevorgyan, T. Tromholt, B. Andreasen, F. C. Krebs, *Adv. Mater.* **2012**, *24*, 580–612.
[10] S. Y. Kook, R. H. Dauskardt, *J. Appl. Phys.* **2002**, *91*, 1293–1303.
[11] M. W. Lane, J. M. Snodgrass, R. H. Dauskardt, *Microelectron Reliab.* **2001**, *41*, 1615–1624.
[12] S. M. Wiederhorn, E. R. Fuller, R. Thomson, *Met. Sci.* **1980**, *14*, 450–458.
[13] M. W. Lane, X. H. Liu, T. M. Shaw, *IEEE T. Device Mater. Re.* **2004**, *4*, 142–147.
[14] B. R. Lawn, *J. Mater. Sci.* **1975**, *10*, 469–480.
[15] R. F. Cook, E. G. Liniger, *J. Am. Ceram. Soc.* **1993**, *76*, 1096–1105.
[16] B. R. Lawn, *Mater. Sci. Eng.* **1974**, *13*, 277–283.
[17] S. M. Wiederhorn, S. W. Freiman, E. R. Fuller, C. J. Simmons, *J. Mater. Sci.* **1982**, *17*, 3460–3478.
[18] G. Greczynski, T. Kugler, W. R. Salaneck, *Thin Solid Films* **1999**, *354*, 129–135.
[19] G. Greczynski, T. Kugler, M. Keil, W. Osikowicz, M. Fahlman, W. R. Salaneck, *J. Electron Spectrosc.* **2001**, *121*, 1–17.
[20] U. Lang, E. Muller, N. Naujoks, J. Dual, *Adv. Funct. Mater.* **2009**, *19*, 1215–1220.
[21] A. M. Nardes, M. Kemerink, R. A.J. Janssen, J. A.M. Bastiaansen, N. M.M. Kiggen, B. M.W. Langeveld, A. J. J. M. van Breemen, M. M. de Kok, *Adv. Mater.* **2007**, *19*, 1196–+.
[22] M. P. de Jong, L. J. van IJzendoorn, M. J. A. de Voigt, *Appl. Phys. Lett.* **2000**, *77*, 2255–2257.
[23] A. G. Macdiarmid, J. C. Chiang, A. F. Richter, A. J. Epstein, *Synthetic Met.* **1987**, *18*, 285–290.
[24] J. P. Yang, Y. J. Yang, J. A. Hou, X. Zhang, W. Zhu, M. Xu, M. X. Wan, *Polymer* **1996**, *37*, 793–798.
[25] J. O. Iroh, K. Levine, *Eur. Polym. J.* **2002**, *39*, 1547–1550.
[26] U. Lang, N. Naujoks, J. Dual, *Synthetic Met.* **2009**, *159*, 473–479.
[27] Y. Matsuda, S. W. King, J. Bielefeld, J. Xu, R. H. Dauskardt, *Acta Mater.* **2012**, *60*, 682–691.
[28] B. M. Sharratt, L. C. Wang, R. H. Dauskardt, *Acta Mater.* **2007**, *95*, 3601–3609.
[29] G. A. Jeffrey, *An introduction to hydrogen bonding*, Oxford University Press, New York, **1997**.
[30] E. P. Guyer, M. Patz, R. H. Dauskardt, *J. Mater. Res.* **2006**, *21*, 882–894.
[31] R. M. Mcmeeking, A. G. Evans, *J. Am. Ceram. Soc.* **1982**, *65*, 242–246.
[32] B. Budiansky, J. W. Hutchinson, J. C. Lambropoulos, *Int. J. Solids Struct.* **1983**, *95*, 337–355.
[33] J. W. Hutchinson, *Acta Metall. Mater.* **1987**, *35*, 1605–1619.
[34] D. B. Marshall, M. C. Shaw, R. H. Dauskardt, R. O. Ritchie, M. J. Readey, A. H. Heuer, *J. Am. Ceram. Soc.* **1990**, *73*, 2659–2666.
[35] H. Okuzaki, H. Suzuki, T. Ito, *J. Phys. Chem. B* **2009**, *113*, 11378–11383.
[36] M. C.A. Garcia, J. L. Balenzategui, *Renew. Energ.* **2004**, *29*, 1997–2010.
[37] E. Voroshazi, B. Verreet, A. Buri, R. Muller, D. Di Nuzzo, P. Heremans, *Org. Electron.* **2011**, *12*, 736–744.
[38] M. F. Kanninen, *Int. J. Fracture* **1973**, *9*, 83–92.